CONSTRAINED REDUCED-ORDER MODELS BASED ON PROPER

ORTHOGONAL DECOMPOSITION

Sohail R. Reddy^a*, Brian A. Freno^{b±}, Paul G.A. Cizmas^b, Seckin Gokaltun^c, Dwayne

McDaniel^c, George S. Dulikravich^a

^aDepartment of Mechanical and Materials Engineering, MAIDROC Laboratory, Florida

International University, 10555 W. Flagler St., Miami, FL 33174, USA

^bDepartment of Aerospace Engineering, Texas A&M University, College Station, TX,

USA

^cApplied Research Center, Florida International University, 10555 W. Flagler St., Miami,

FL 33174, USA

*Corresponding Author: Tel. +1 352 2138933

E-mail address: sredd001@fiu.edu (S.R. Reddy)

ABSTRACT

A novel approach is presented to constrain reduced-order models (ROM) based on proper

orthogonal decomposition (POD). The Karush-Kuhn-Tucker (KKT) conditions were

applied to the traditional reduced-order model to constrain the solution to user-defined

± Currently: Sandia National Laboratories

*Corresponding Author: Tel. +1 352 2138933

E-mail address: sredd001@fiu.edu (S.R. Reddy)

bounds. The constrained reduced-order model (C-ROM) was applied and validated against the analytical solution to the first-order wave equation. C-ROM was also applied to the analysis of fluidized beds. It was shown that the ROM and C-ROM produced accurate results and that C-ROM was less sensitive to error propagation through time than the ROM.

Keywords: Proper Orthogonal Decomposition, Reduced-Order Modeling, Karush-Kuhn-Tucker, Multiphase Flows, Computational Fluid Dynamics, Fluidized Beds

INTRODUCTION

A great deal of effort has been dedicated to develop reduced-order models (ROMs) of numerical methods that can provide accurate predictions while dramatically reducing computational time for a wide range of applications covering fluid mechanics, heat transfer, structural dynamics [1] and electromagnetics [2]. The challenges posed by the different engineering fields have led to various types of reduced-order models. A common approach for model order reduction is through projection. Some of the methodologies for model reduction include balanced truncation [3], trajectory piecewise-linear approach [4] and proper orthogonal decomposition.

Reduced-order models based on proper orthogonal decomposition have been successfully implemented to reduce computational cost while maintaining high fidelity solutions. Proper orthogonal decomposition (POD) is a method by which an optimal set of spatial basis function can be extracted from the solution of the full-order model (FOM).

The set of partial differential equations are then projected onto the basis functions using Galerkin projection, resulting in a smaller system of ordinary differential equations. Recent reviews of ROMs based on POD are presented by Beran and Silva [5], Dowell and Tang [6] and Lucia *et al.* [7].

POD has been successfully used in conjunction with finite element, finite volume and finite difference methods for model reduction. Wang *et al.* [8] used a mixed finite element method with POD basis functions to solve the transient Navier-Stokes equations. Fic *et al.* [9] projected the finite element discretized heat conduction equation onto the POD basis functions to develop a reduced-order model for non-linear heat conduction. Yuan *et al.* [10] used a finite volume discretized system of PDEs and POD to developed reduced-order model for bubbling fluidized beds. Luo *et al.* [11, 12] used POD to reduce a finite difference extrapolation algorithm to obtain solutions to a Lighthill, Whitham and Richards (LWR) traffic flow model and two-dimensional shallow water equations.

Over the last decade, much attention has been dedicated to: i) modeling of off-reference conditions, ii) modeling moving/deforming meshes, and iii) acceleration techniques and robustness.

Modeling of off-reference conditions can be performed by direct interpolation, enriching the snapshot database, interpolation of basis functions within the tangent space to the Grassman manifold [13, 14] and modification of basis functions using sensitivity analysis [15]. Some of these methods are reviewed by Vertrano *et al.* [16].

The advances in modeling of deforming meshes have primarily been driven by aeroelastic and fluid-structure interaction applications. Bogaers *et al.* [17] formulated an efficient mesh movement method based on POD. Freno and Cizmas [18] and Freno *et al.*

[19] presented a POD decomposition method for nonlinear flows with deforming meshes which applied dynamic basis functions for modeling of flows.

Several acceleration techniques for reduced-order model based on POD were investigated by Cizmas *et al.* [20], which resulted in the reduction of computational time by a factor of 114. Brenner *et al.* [21] investigated two approaches for constructing the autocorrelation matrix, showing that a split approach results in much lower errors than the coupled approach. Brenner *et al.* [22] also formulated an augmented POD method capable of resolving discontinuity in the solution, although this work needs to be generalized for 2D and 3D cases. Alonso *et al.* [23] developed a robust reduced-order model that is independent of the way the snapshots were computed to analyze a classical fluid mechanics test case of a flow over a backward facing step.

This work modifies the traditional reduced-order model based on POD to constrain the solution within user-defined bounds. Robust reduced-order models are needed to cope with issues such as error arising from numerically solving the eigenvalue problem to obtain the POD basis functions and errors in snapshots taken from the full order model. This robust model is developed by applying the Karush - Kuhn - Tucker (KKT) conditions to the existing POD based ROM.

PROPER ORTHOGONAL DECOMPOSITION (POD)

Proper orthogonal decomposition, also known as Karhunen – Loeve decomposition, singular value decomposition and principal component analysis, is a procedure for

extracting an optimal set of orthogonal basis functions from a collection of snapshots. POD is able to detect the underlying structure of the snapshots.

Let us consider a sequence of experimental or numerical observations of a scalar function $u(x,t_i)$ where i=1,...,M and M is the number of observations. The observations $u(x,t_i)$ are parameterized by time, t_i , where the observation at each time is called a snapshot. Applying POD to the collection of snapshots extracts time independent orthogonal basis functions, referred to as POD modes, $\phi_i(x)$, and time dependent orthogonal coefficients, $\alpha_i(x)$, such that the reconstruct of the snapshots,

$$u(x,t_i) = \sum_{k=1}^{M} \alpha_k(t_i) \phi_k(x) , \qquad i = 1,...,M$$
 (1)

is optimal in the sense that the least square truncation error

$$\varepsilon_{m} = \left\langle \left\| u(x, t_{i}) - \sum_{k=1}^{m} \alpha_{k}(t_{i}) \phi_{k}(x) \right\|^{2} \right\rangle$$
 (2)

(where $||\cdot||^2$ is the L^2 -norm, $\langle \cdot \rangle$ is the average over the number of observations) is minimum for any given number of basis functions, m, over all possible sets of basis functions such that $m \leq M$. The optimum condition specified by Eq. (2) is identical to finding basis functions, ϕ , that maximize the normalized averaged projection of u onto ϕ given by Eq. (3).

$$\max_{\phi \in L^{2}(\Omega)} \frac{\left\langle \left| (u, \phi) \right|^{2} \right\rangle}{\left| \left| \phi \right| \right|^{2}} \tag{3}$$

where $|\bullet|$ denotes the modulus. The optimum condition reduces to [24]:

$$\int_{\Omega} \langle u(x)u^*(y)\rangle \phi(y)dy = \lambda \phi(x)$$
 (4)

The eigenvalues, λ , can be used to determine the energy captured by each eigenfunction. The basis functions $\{\phi_i\}$ are the eigenfunctions of the integral equation Eq. (4), whose kernel function is the autocorrelation function $\langle u(x)u^*(y)\rangle \equiv R(x,y)$. The autocorrelation function, R(x,y), is replaced by the tensor product matrix

$$\overline{\overline{R}}(\mathbf{x}, \mathbf{y}) = \frac{1}{M} \sum_{i=1}^{M} u(\mathbf{x}, t_i) u^T(\mathbf{y}, t_i)$$
 (5)

where $u(\mathbf{x},t_i) = [u(x_1,t_i),u(x_2,t_i),...,u(x_N,t_i)]^T$ are vector – valued functions and N is the resolution of the spatial domain. The eigenfunctions, $\phi_i(\mathbf{x})$, can be found by solving the eigenvalue problem defined by Eq. (6).

$$\overline{\overline{R}}(\mathbf{x}, \mathbf{y})\phi(\mathbf{x}) = \lambda\phi(\mathbf{y}) \tag{6}$$

The eigenvalue problem defined by Eq. (6) is often too computationally expensive as the problem is of size $N \times N$. For this reason the method of snapshots is used to reduce the $N \times N$ to a much smaller $M \times M$ sized problem.

METHOD OF SNAPSHOTS

The method of snapshots was first proposed by Sirovich [25], in which the size of the eigenvalue problem defined by Eq. (6) is reduced to a much smaller dimension problem. Since the eigenfunctions, ϕ_i , and data vectors u_i span the same linear space [24, 25], it allows the eigenfunctions to be represented as a linear combination of the data vector

$$\phi_i = \sum_{k=1}^M v_k^i \mathbf{u}_k , \qquad i = 1, ..., M$$
 (7)

Substituting Eq. (7) into Eq. (6) yields a much smaller eigenvalue problem as shown below

$$C\mathbf{v} = \lambda \mathbf{v} \tag{8}$$

where $\mathbf{v}^k = (v_1^k, ..., v_M^k)$ is the k^{th} eigenvector of Eq. (8) and C is a symmetric $M \times M$ matrix defined by $\left[c_{ij}\right] = (1/M)(\mathbf{u}_i, \mathbf{u}_j)$. Here, $(\mathbf{u}_i, \mathbf{u}_j)$ is the standard vector inner

product, $(\mathbf{u}_i, \mathbf{u}_j) = u(x_1, t_i)u(x_1, t_j) + ... + u(x_N, t_i)u(x_N, t_i)$. The eigenvectors of Eq. (8) can then be used to reconstruct the eigenfunctions of Eq. (6) as Eq. (7). The computed eigenfunctions were then normalized and reordered according to decreasing eigenvalues as $\lambda_1 > \lambda_2 > ... > \lambda_M = 0$. The energy captured by each eigenfunction is then computed as

$$E_i = \frac{\lambda_i}{\sum_{k=1}^{M} \lambda_k} \tag{9}$$

REDUCED FIRST-ORDER WAVE EQUATION

The constrained reduced order methodology is first applied to a simple first–order wave equation. In this work the analytical form of the first-order wave equation was reduced although discretized forms of the equation can also be used. The first-order wave equation is given by Eq. (10) as

$$\frac{\partial u}{\partial t} + c \frac{\partial u}{\partial x} = 0, \qquad x \in [0,1], \qquad c > 0$$
(10)

with the initial condition

$$u(x,0) = f(x) \ge 0 \tag{11}$$

for which the analytical solution is

$$u(x,t) = f(x - ct) \tag{12}$$

where f(x) satisfies the initial condition. Let us represent u(x,t) as a linear combination of POD modes

$$u(x,t) \approx \sum_{k=1}^{m} \alpha_k(t)\phi_k(x)$$
 (13)

Here, m is the number of modes used in the POD approximation. Substituting Eq. (13) into Eq. (10) and using the Einstein summation convention yields a set of ordinary differential equations

$$\dot{\alpha}_i \phi_i + c \alpha_i \phi_i = 0 \tag{14}$$

where • denotes time derivations and ' denotes spatial derivatives. Applying Galerkin projection to Eq. (14) yields

$$\int_{0}^{1} \alpha_{i} \phi_{i} \phi_{j} dx + \int_{0}^{1} c \alpha_{i} \phi_{i}^{\dagger} \phi_{j} dx = 0$$

$$\tag{15}$$

which, due to the orthonormality of the POD modes, reduces to

$$\dot{\alpha}_i + c \left(\int_0^1 \phi_i \dot{\phi}_j \, dx \right) \alpha_i = 0 \tag{16}$$

This can be written in vector form as

$$\dot{\underline{\alpha}} + \mathbf{B}\underline{\alpha} = 0 \tag{17}$$

where $\underline{\alpha} \in \mathbb{R}^m$ and $\mathbf{B} \in \mathbb{R}^{m \times m}$. The elements of matrix \mathbf{B} are

$$B_{ij} = c \left(\int_{0}^{1} \phi_i \phi_j \, dx \right) \tag{18}$$

Using an implicit time integration scheme, Eq. (17) becomes

$$(I + \Delta t \mathbf{B}) \underline{\alpha}^{n+1} - \underline{\alpha}^{n} = 0$$
 (19)

where I is the identity matrix of rank m, Δt is the time step and $\underline{\alpha}^n := \underline{\alpha}(t^n)$. With the notation $C = I + \Delta t \mathbf{B}$, Eq. (19) becomes

$$\mathbf{C}\underline{\alpha}^{n+1} - \underline{\alpha}^{n} = 0 \tag{20}$$

The time coefficients for each time step can be found by solving Eq. (20).

KARUSH – KUHN – TUCKER (KKT) CONDITIONS

The Karush-Kuhn-Tucker (KKT) conditions are heavily used in mathematical optimization problems. They represent a series of necessary conditions for a solution in nonlinear programming to be optimal while satisfying constraints. Effectively, they extend the method of Lagrange multipliers, which only allow equality constraints, to account for inequality constraints.

Consider a nonlinear single-objective optimization problem

minimize
$$f(x)$$

subject to $h_i(x) = 0$ $i = 1,...,m$

$$g_i(x) \le 0 \quad j = 1,...,l$$
(21)

where f is the objective and $h_i(x)=0$, i=1,...,m and $g_j(x)\leq 0$, j=1,...,l are m equality constraints and l inequality constraints, respectively. Let us assume that the objective function and the constraints are continuously differentiable at x^* . Then, there exist constants μ_i (where i=1,...,m) and λ_j (where j=1,...,l) called the KKT multipliers, that satisfy the following conditions [26]

$$\nabla f(x^*) + \sum_{i=1}^{m} \mu_i \nabla h_i(x^*) + \sum_{i=1}^{l} \lambda_j \nabla g_j(x^*) = 0$$
 (22)

$$h_i(x^*) = 0$$
, $i = 1,...,m$ and $g_i(x^*) \le 0$, $j = 1,...,l$ (23)

$$\lambda_i \ge 0 \;, \; j = 1, \dots, l \tag{24}$$

$$\lambda_j g_j(x^*) = 0, \ j = 1,...,l$$
 (25)

Equations (22), (23), (24) and (25) are referred to as stationary, primal feasibility, dual feasibility and complementary slackness, respectively. When no inequality constraints are present, the KKT conditions decompose to the Lagrange conditions and the KKT multipliers are called the Lagrange multipliers.

CONSTRAINED REDUCED-ORDER MODEL (C-ROM)

The constrained reduced-order model in this work is developed by applying the KKT conditions to the POD-based reduced-order model. It should be mentioned that only inequality constraints are considered in this work, however this procedure can be extended to handle equality constraints as well. Further model development will only consider inequality constraints. To apply the KKT conditions, the Lagrangian must first be constructed as follows:

$$L = f(x) + \sum_{i=1}^{m} \mu_i h_i(x) + \sum_{j=1}^{l} \lambda_j g_j(x)$$
 (26)

Using the linear system defined by Eq. (20), the function to minimize becomes

$$\left\| \mathbf{C} \underline{\alpha}^{n+1} - \underline{\alpha}^{n} \right\|^{2} \tag{27}$$

subject to
$$u(x,t) = \mathbf{\Phi}\underline{\alpha}^{n+1} \ge 0$$
 (28)

where $\Phi = [\underline{\phi}_1 ... \underline{\phi}_m]$, $\Phi \in \mathbb{R}^{N \times m}$ is the matrix of POD modes, N is the number of spatial points. The Lagrangian is then constructed as

$$L = \left\| \mathbf{C} \underline{\alpha}^{n+1} - \underline{\alpha}^{n} \right\|^{2} + \lambda^{T} \mathbf{\Phi} \underline{\alpha}^{n+1}$$
(29)

The stationary condition Eq. (22) then results in

$$L_{\alpha^{n+1}} = 2\mathbf{C}^T \mathbf{C} \underline{\alpha}^{n+1} - 2\mathbf{C}^T \underline{\alpha}^n + \mathbf{\Phi}^T \underline{\lambda}$$
(30)

The complementary slackness, after forcing Eq. (28) as a binding constraint, yields

$$\mathbf{\Phi}\underline{\alpha}^{n+1} = 0 \tag{31}$$

The time coefficients and KKT multipliers can be obtained by solving the system of equations

$$\begin{pmatrix}
2\mathbf{C}^{T}\mathbf{C} & \mathbf{\Phi}^{T} \\
\mathbf{\Phi} & 0
\end{pmatrix}
\begin{cases}
\underline{\alpha}^{n+1} \\
\underline{\lambda}
\end{cases} =
\begin{cases}
2\mathbf{C}^{T}\underline{\alpha}^{n} \\
0
\end{cases}$$
(32)

This approach was used to solve Eq. (10) with initial condition Eq. (11) where $f(x) = x^2$.

To mimic errors encountered in large simulations where errors affect both the full order model and the POD modes, two errors were introduced in the model: 1) the function $f(x) = x^2$ was replaced by $f(x) = x^2 - \varepsilon$ and 2) the POD modes were perturbed by some error, ε . The first error mimics the truncation and/or round-off error in the full order model simulation. In this case the solution becomes negative near x = 0. The second error mimics the error in the eigenvalue algorithm for evaluating the POD modes.

RESULTS OF C-ROM APPLIED TO FIRST-ORDER LINEAR WAVE EQUATION

The results of the unconstrained and constrained reduced-order model subjected to the defined constraints are presented in this section. The spatial discretization used a constant interval of 0.01 such that N=100 and the temporal discretization used a constant interval of 0.005 such that M=200. Because N < M, the POD modes were directly obtained by solving the eigenvalue problem defined by Eq. (6) and not by using the method of

snapshots. The wave speed, c, was held constant at 5. The number of POD modes, m, used for the reconstruction and the level of error, ε , introduced is varied.

Figure 1 shows the solution to the first-order linear wave equation for $\varepsilon = 10^{-4}$. It can be seen that the unconstrained POD reduced-order model gives negative results near x = 0 and therefore violates the constraint given by Eq. (28).

The constrained reduced-order model, however, satisfied the constraint and produced a non-negative solution throughout the spatial domain.

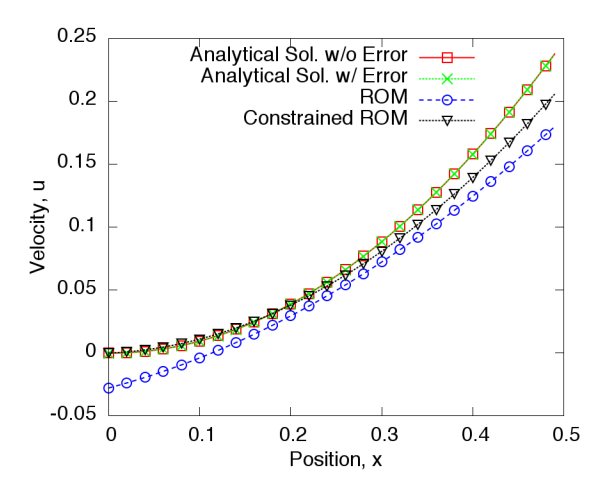


Figure 1: Solution obtained using ROM and C-ROM for $\varepsilon = 10^{-4}$ and m = 3

Figure 2 shows the solution to Eq. (10) when $\varepsilon = 10^{-2}$. It can be seen that despite the increased error, the constrained ROM is still able to produce a non-negative solution unlike the unconstrained ROM. As expected, the increase in error drives the reduced-order model further away from the analytical solution. Increasing the error has a more profound effect on the unconstrained ROM than the constrained ROM, as can be seen in the increase in

negativity of the solution near x = 0. The difference between the ROM solutions with two different errors levels was on the order of 10^{-2} .

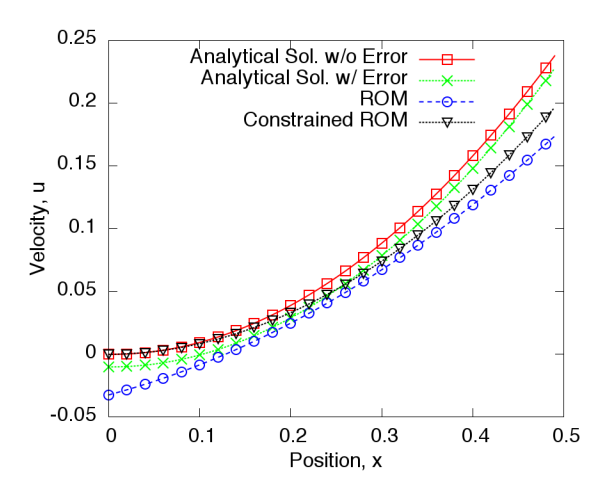


Figure 2: Solution obtained using ROM and C-ROM for $\varepsilon = 10^{-2}$ and m = 3

It should be noted that three POD modes were enough to accurately reconstruct the solutions for the error levels used in Fig. 1 and Fig. 2.

As with all transient simulations, error can propagate through and compound over the temporal domain. It can often lead to nonphysical results and even divergence of the solution. This error can be due to error in the solution initialization and accuracy of the temporal discretization. The effects of this error propagation through time on the constrained and unconstrained reduced-order model are investigated next.

Figure 3 shows the results obtained using the unconstrained and constrained reduced-order model at three time steps, where $\varepsilon = 10^{-2}$, using seven POD modes. It can be seen that both the unconstrained ROM and C-ROM tend away from the analytical solution as we advance in time. It also shows that the unconstrained ROM diverges much sooner than

the constrained ROM. Despite the propagation of error, the C-ROM is able to satisfy the constraint at each of the three time-steps. It can be seen from Eq. (12) and Fig. 3 that even the analytical solution containing errors becomes negative as we progress in time. The C-ROM however is still able to produce a non-negative solution.

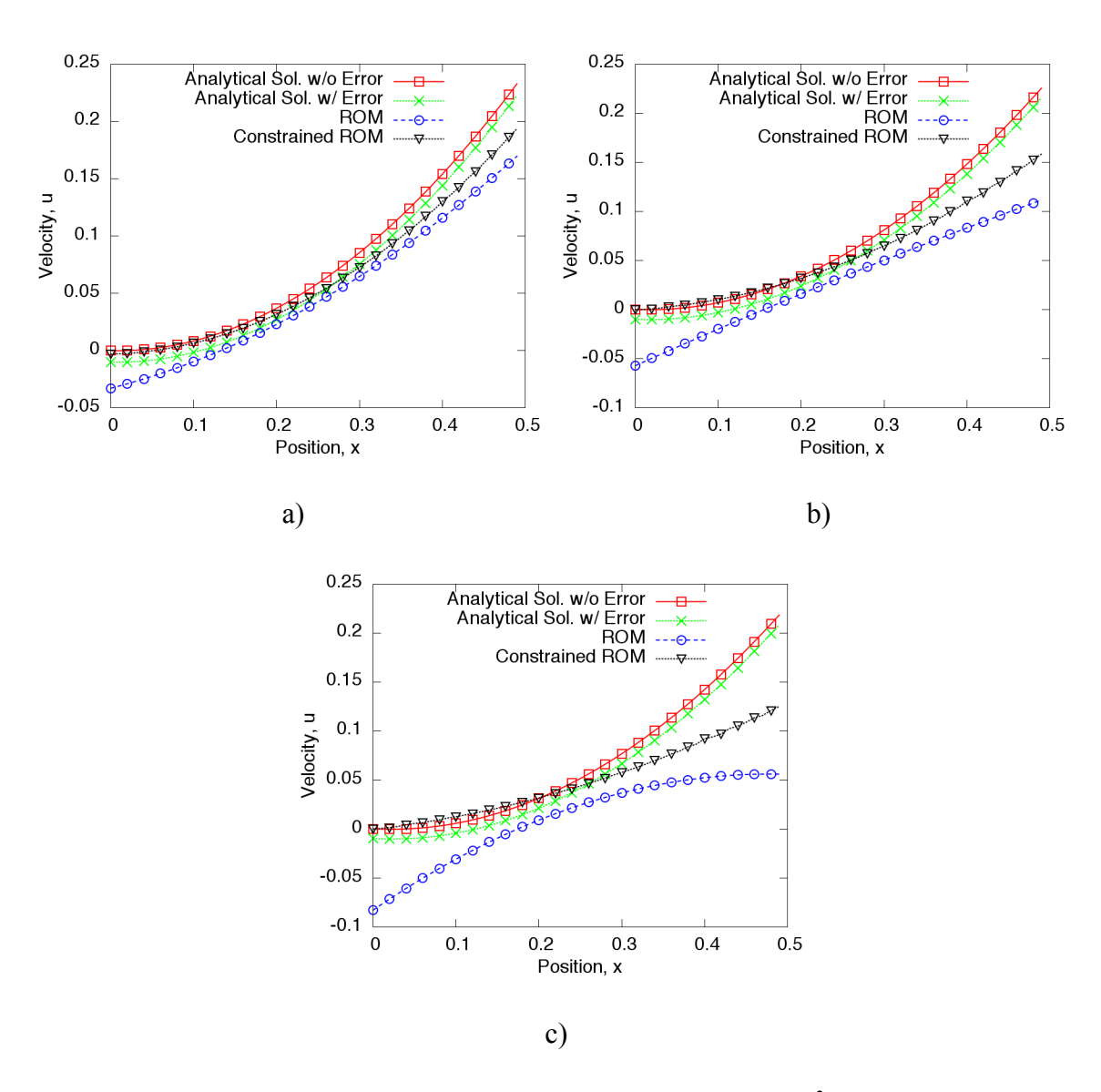


Figure 3: Solution obtained using ROM and C-ROM for $\varepsilon = 10^{-2}$, $\Delta t = 0.0005$ and m = 7 at a) $t = 4\Delta t$, b) $t = 7\Delta t$, and c) $t = 10\Delta t$

C – ROM APPLIED TO FLUIDIZATION PROBLEMS

The C-ROM has shown to satisfy user-defined constraints that the traditional ROM violates. It can, therefore be applied to constrain solutions for much more difficult, non-linear problems. One such problem was presented by Brenner *et al.* [22] where the gas void fraction, upon reconstruction, exceeds the upper bound of one.

The original reduced-order model based on POD for a bubbling, isothermal fluidized bed was developed by Yuan *et al.* [10] and Cizmas *et al.* [20]. The ROM was developed by projecting the finite volume discretized equations of a fluidized bed used by MFIX software [27] onto the POD modes. The complete set of governing equations, mass and momentum balance, are given in Appendix A. Unlike MFIX, which solves the solids mass balance equation, the ROM solves the gas void fraction correction equation

$$a_P^{\varepsilon_s} \varepsilon_{sP}' = \sum_{nb} a_{nb}^{\varepsilon_s} \varepsilon_{snb}' + b_P^{\varepsilon_s}$$
(33)

Using the POD representation of the void fraction defined by

$$\varepsilon_{g}(x,t) = \phi_{0}(x) + \sum_{k=1}^{m^{\varepsilon_{s}}} \alpha_{k}^{\varepsilon'}(t) \phi_{k}(x)$$
(34)

Eq. (33) converts to Eq. (35)

$$\left[\tilde{A}^{\varepsilon_{s}}\right]\left\{\alpha^{\varepsilon_{s}'}\right\} = \left\{\tilde{B}^{\varepsilon_{s}}\right\} \tag{35}$$

where

$$\tilde{A}_{lk}^{\varepsilon_s} = \{\phi_l\}^T [A] \{\phi_k\} - \sum_{nb=1}^{NB} \{\phi_l\}^T [A_{nb}] \{\phi_{k_{nb}}\}, \quad l, k = 1, ..., m$$
(36)

$$\tilde{B}_{l}^{\varepsilon_{s}} = \left\{ \phi_{l} \right\}^{T} \left\{ b \right\}, \qquad l = 1, ..., m \tag{37}$$

Replacing $\tilde{B}^{\varepsilon_s}$ with $-\tilde{B}^{\varepsilon_s}$ is analogous to $\tilde{B}^{\varepsilon_s}$ which then solves for the gas void fraction correction. The formulation in this work corrects the gas void fraction and not the solids volume fraction. A more detailed derivation is given in [10] and [20] and Appendix B.

Figure 4 shows the first five POD modes of the gas void fraction extracted using the method of snapshots for the case given by Brenner *et al.* [22]. A full description of the test case is given in Appendix C. It is known that the time coefficients can be analytically computed for a particular snapshot by projecting the POD modes onto the snapshot, Eq. (47). It was shown in [22] that when insufficient number of POD modes are used, even the analytically computed time coefficients will violate the physical constraints. Figure 5 shows the reconstruction of the gas void fraction using various numbers of POD modes and the analytically computed time coefficients. The white areas represent the void fraction exceeding a value of one. It can be seen that increasing the number of modes results in a more accurate reconstruction but still violates the upper limit on the gas void fraction.

Therefore, it is very appealing to develop a C-ROM that could constrain the void fraction by applying the KKT conditions to the volume fraction correction equation.

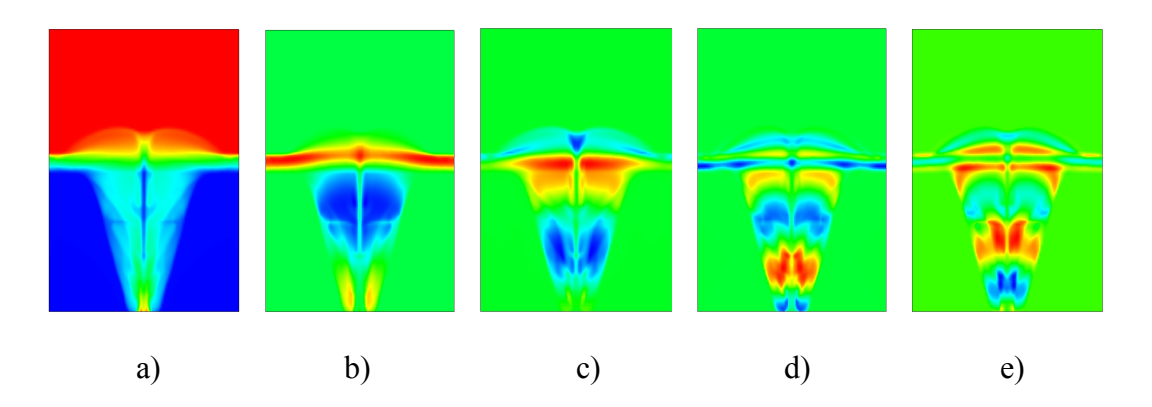


Figure 4: First five POD basis functions extracted for case defined by [22] where: a) ϕ_0 , b) ϕ_1 , c) ϕ_2 , d) ϕ_3 , and e) ϕ_4 .

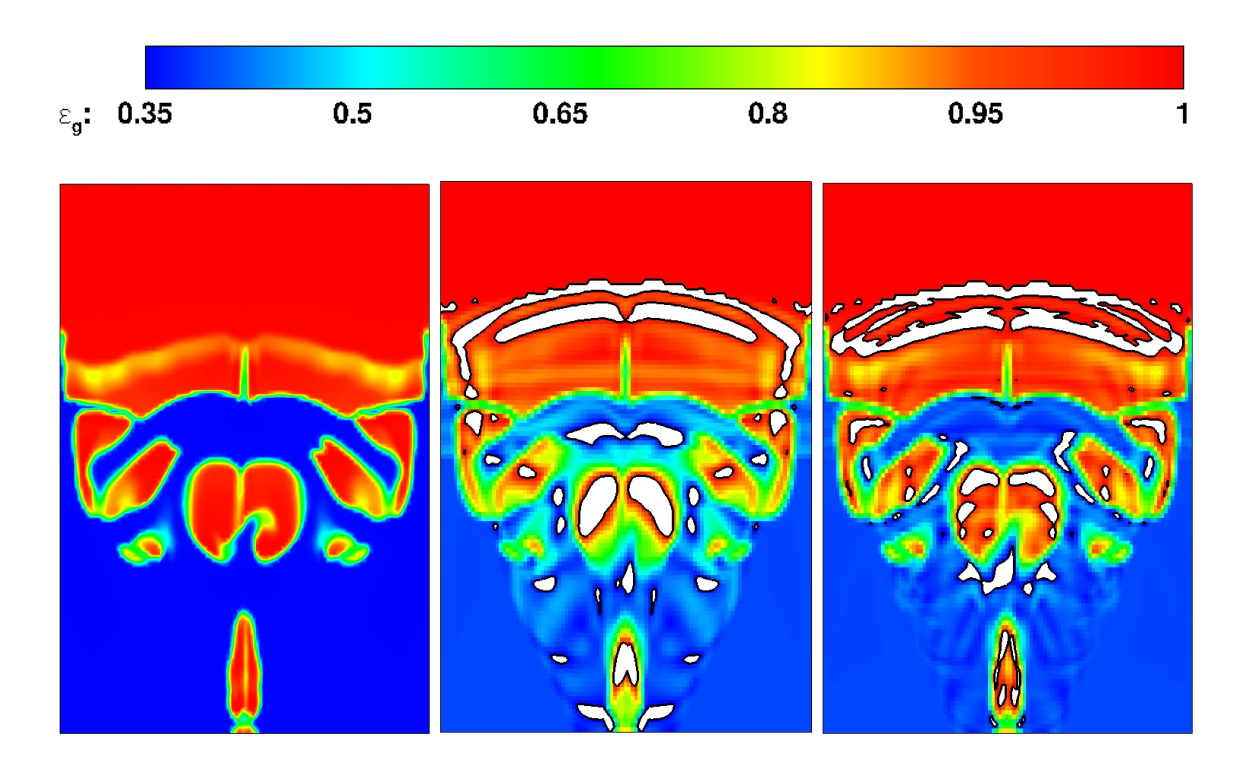


Figure 5: Gas void fraction at t = 1s of two-dimensional bubbling fluidized bed defined by [18]: a) full-order model, b) POD reconstruction with 16 modes, c) POD reconstruction with 32 modes (white areas represent outside the bounds ε_g [0.35, 1.0])

DERIVATION OF A C-ROM FOR FLUIDIZED BED FLOWS

As before, the KKT conditions can then be applied to Eq. (35) to develop a C-ROM for fluidized beds where the function to minimize becomes

$$J = \left\| \tilde{A}^{\varepsilon_s} \alpha^{\varepsilon_s} - \tilde{B}^{\varepsilon_g} \right\|^2 \tag{38}$$

subject to
$$\varepsilon_g \le 1.0$$
 (39)

The ROM developed [20] corrects the void fraction as

$$\varepsilon_{g}(x,t) = \varepsilon_{g}^{*}(x) + \varepsilon_{g}(x,t) \tag{40}$$

where $\phi_0(x)$ and $\varepsilon_g^*(x)$ are assumed to be equal. Combining Eq. (40) and Eq. (34) yields

$$\varepsilon_{g}(x,t) = \sum_{k=1}^{m^{\varepsilon_{s}}} \alpha_{k}^{\varepsilon_{g}}(t) \phi_{k}(x)$$
(41)

Using Eq. (40) and Eq. (41), the constraint Eq. (39) becomes

$$\varepsilon_{\varrho}^{*}(x) + \Phi(x)\alpha_{\varrho}(t) - 1.0 \le 0 \tag{42}$$

where $\Phi = [\underline{\phi}_1 ... \underline{\phi}_m]$, $\Phi \in \mathbb{R}^{N \times m}$ is the matrix of POD modes, $\alpha_g \in \mathbb{R}^m$ is the vector of time coefficients for the void fraction correction, and N is the number of spatial points. Then using Eq. (38) and Eq. (42), the Lagrangian can be constructed as

$$L = \left\| \tilde{A}^{\varepsilon_s} \alpha^{\varepsilon_g} - \tilde{B}^{\varepsilon_g} \right\|^2 + \lambda^T \left(\varepsilon_g^* + \Phi \alpha_g' - 1.0 \right)$$
 (43)

The stationary condition yields

$$L_{\alpha} = 2(\tilde{A}^{\varepsilon_{s}})^{T} \tilde{A}^{\varepsilon_{s}} \alpha^{\varepsilon_{s}} - 2(\tilde{A}^{\varepsilon_{s}})^{T} \tilde{B}^{\varepsilon_{s}} + \Phi^{T} \lambda = 0$$
(44)

The complementary slackness yields

$$\varepsilon_g^* + \Phi \alpha^{\varepsilon_g} - 1.0 = 0 \tag{45}$$

The time coefficients and the KKT multipliers can be obtained by solving

$$\begin{pmatrix}
2(\tilde{A}^{\varepsilon_s})^T \tilde{A}^{\varepsilon_s} & \Phi^T \\
\Phi & 0
\end{pmatrix}
\begin{cases}
\underline{\alpha}^{\varepsilon_g} \\
\underline{\lambda}
\end{cases} = \begin{cases}
2(\tilde{A}^{\varepsilon_s})^T \tilde{B}^{\varepsilon_g} \\
1.0 - \varepsilon_g^*
\end{cases}$$
(46)

A detailed derivation is given in Appendix D.

VALIDATION OF C-ROM FOR FLUIDIZED BEDS

The existing ROM model for fluidized beds was already validated against the full order model in previous works [10, 20]. Here, the developed C-ROM model is compared against the existing ROM. The test case chosen is the gas-solids flow test case used by Yuan *et al.* [10]. Because the difference in solution from the two different systems of equations, Eq. (35) and Eq. (46) was being studied, no artificial error was introduced to either the ROM or C-ROM. The simulation was run from t = 0.2 s to t = 1 s. The total number of grid points was N = 13392 and a total of M = 320 snapshots were used to extract the POD basis functions. Table 1 shows the number of POD modes used for each variable

Table 1: Number of POD modes used to validate C-ROM

| $oldsymbol{\mathcal{E}}_{g}$ | p_{g} | u_g | v_g | u_s | V_s |
|------------------------------|---------|-------|-------|-------|-------|
| 4 | 3 | 10 | 7 | 7 | 4 |

Figures 6 and 7 show the distribution of the six field variables computed using ROM and C-ROM, respectively. It shows that the solutions obtained from the two solvers produced similar results.

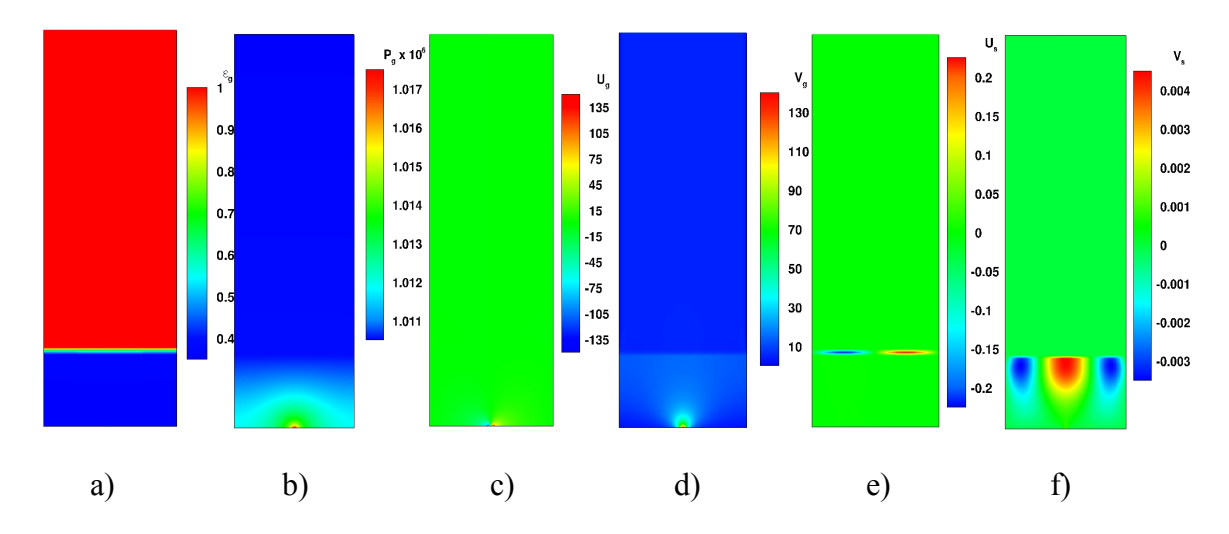


Figure 6: Distribution obtained using FOM at t = 1s for: a) ε_g , b) $p_g \times 10^6$, c) u_g , d) v_g , e) u_s , and f) v_s .

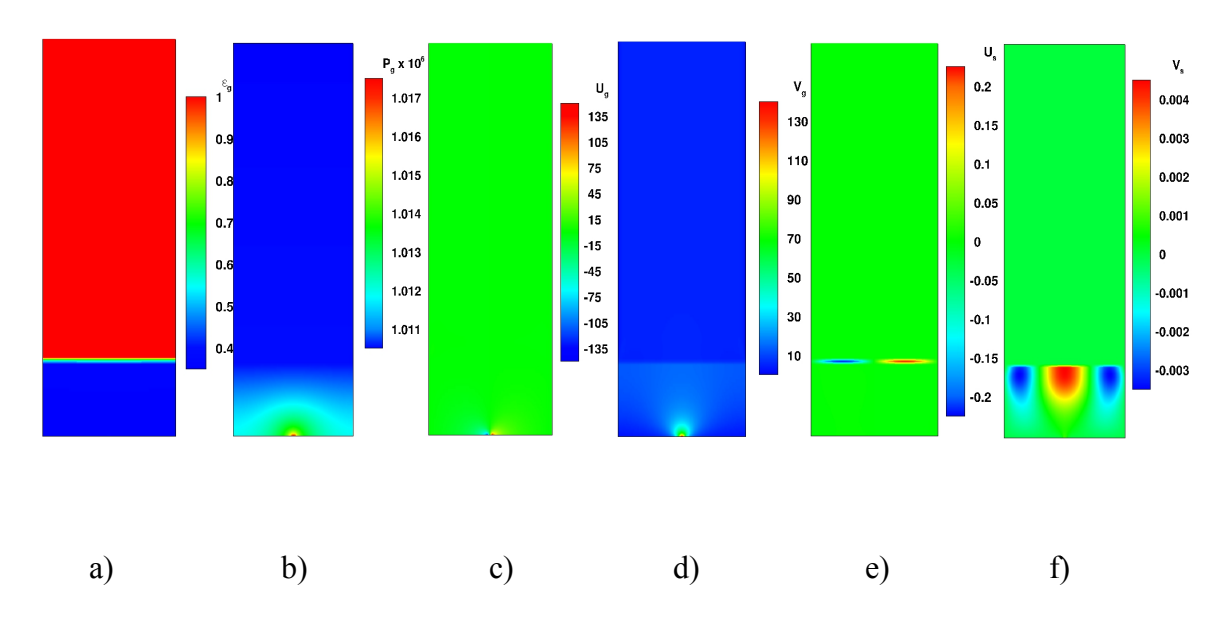
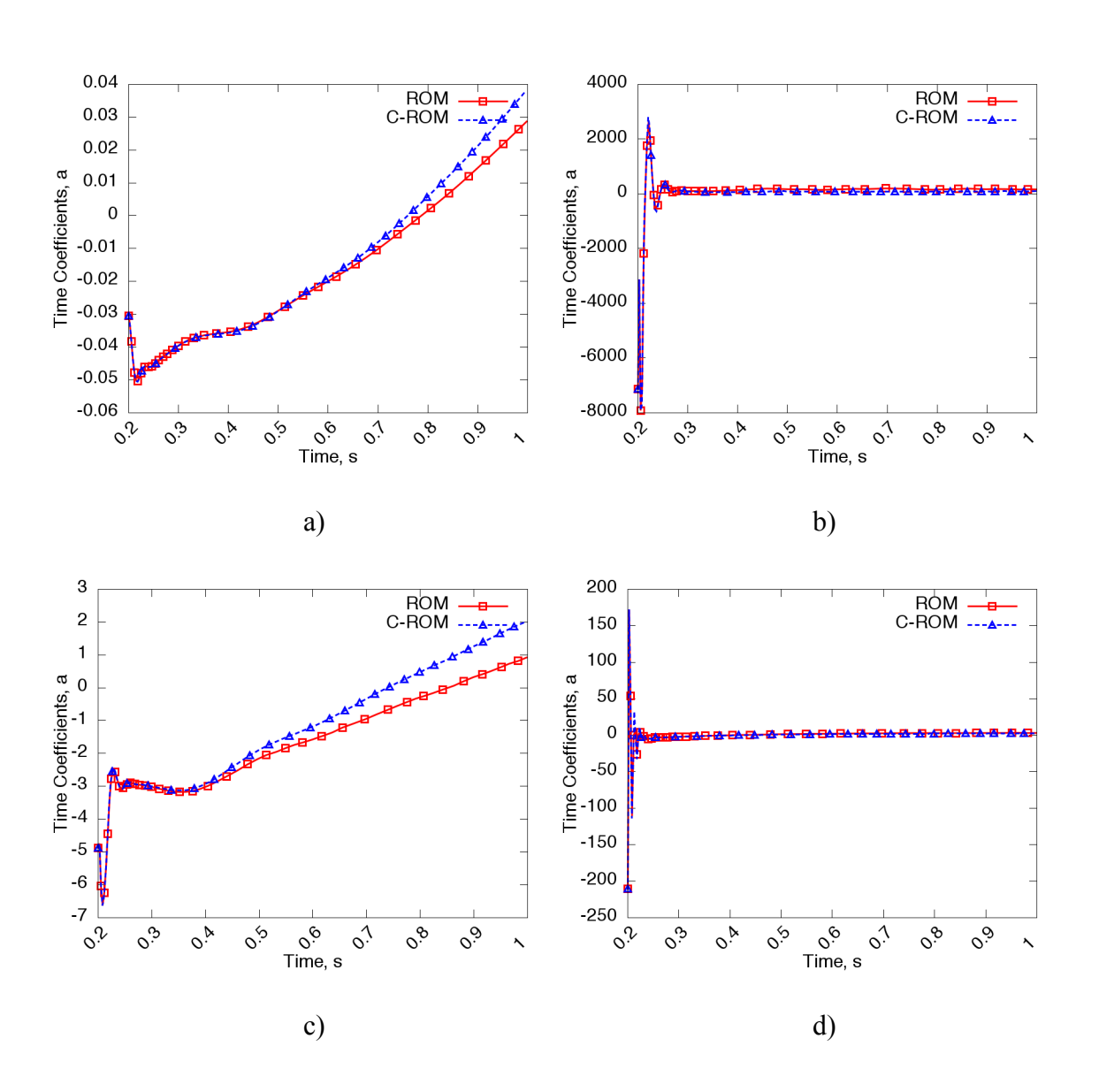


Figure 7: Distribution obtained using C-ROM at t = 1s for: a) ε_g , b) $p_g \times 10^6$, c) u_g , d) v_g , e) u_s , and f) v_s .

Figure 8 shows the time coefficients computed using ROM and C-ROM for the first mode of the six field variables. Only the first POD mode is shown as it captures the most

energy, but it can be reported that the conclusion applies to the time coefficients for all the modes. It can be seen that the time coefficients obtained from the ROM and C-ROM are similar at each time step. This was observed for each mode used to represent the six field variables. It shows that when no error is present in the ROM, the two systems of equations, Eq. (35) and Eq. (46), produce similar results.



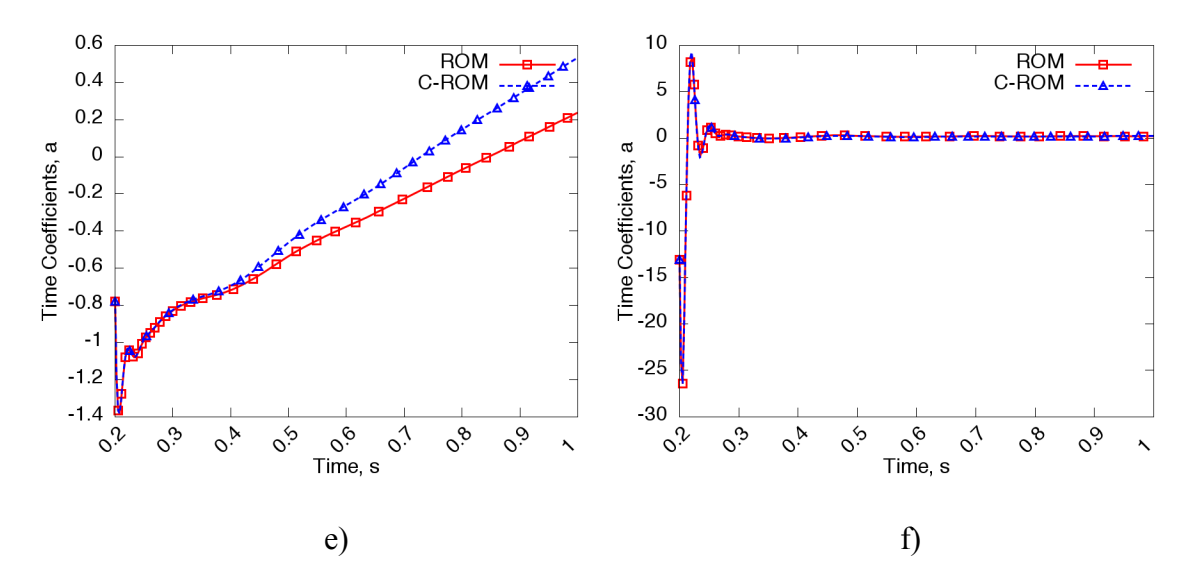


Figure 8: Time coefficients obtained from ROM and C-ROM for the first POD mode of: a) ε_g , b) p_g , c) u_g , d) v_g , e) u_s , and f) v_s .

The comparison of the computing time for the entire analysis is meaningless, as Eq. (46) only needs to be solved when the void fraction exceeds the user-specified limits. However, the times required to solve Eq. (35) and Eq. (46) can be compared (Table 2). It can be seen that the solution of the void fraction equation when KKT is implemented is of the same order of magnitude as the solution time needed to solve FOM. For this reason Eq. (46) should only be solved when the void fraction constraint is violated.

Table 2: Computing times for the FOM, ROM and C-ROM system

| | FOM | ROM | C-ROM |
|----------|-------|------|-------|
| Time (s) | 0.003 | 8E-6 | 0.003 |

A workstation computer with the Ubuntu 14.04 LTS Linux OS was used for this simulation. All simulations were run on a single core of an Intel Core i7, 3.4 GHz with 64 GB of allocated memory.

APPLICATION OF C-ROM TO CONSTRAIN GAS VOID FRACTION

It has been proven that the solution obtained by C-ROM matches that obtained using ROM and FOM when no artificial errors are introduced. The C-ROM in its current state is not able to cope with errors that are too small to cause a constraint violation. That is, the KKT conditions only apply when errors are large enough that the computed time coefficients lead to a constraint violation. For this reason, a test case where the void fraction went out of bound was selected for study. The case chosen is that presented in [22] where the central jet speed in this study was $v_1 = 198.8 \, \text{cm/s}$. The central jet speed was chosen as it lead to mild fluidization. The number of grid points and snapshots were the same as in the case for validation of C-ROM. Table 3 shows the number of POD basis functions used for the mild fluidization case.

Table 3: Number of POD modes used for a mild fluidization test case

| $oldsymbol{arepsilon}_{g}$ | p_{g} | u_g | v_g | u_s | v_s |
|----------------------------|---------|-------|-------|-------|-------|
| 33 | 4 | 24 | 25 | 24 | 20 |

When solving this problem using ROM, the void fraction solution exceeded 1.0 at t = 0.252s. It was noticed that the void fraction computed using C-ROM also exceeded 1.0 at t = 0.252s. It was expected that the C-ROM would compute time coefficients that do not violate the constraint. Further investigation of the snapshot identified the issue. It is known that the time coefficients for the snapshots for each mode can be computed as

$$\mathbf{a} = \mathbf{\Phi}^T \mathbf{U} \tag{47}$$

where $\mathbf{a} \in \mathbb{R}^{m \times M}$ is the matrix of time coefficients, $\Phi \in \mathbb{R}^{N \times m}$ is a matrix of POD modes and $\mathbf{U} \in \mathbb{R}^{N \times M}$ is the matrix of collection of snapshots. These are the analytically computed time coefficients that best reconstruct the data vectors. These time coefficients can then again be used to reconstruct the data vectors using Eq. (47). This reconstruction will not be exact unless all modes are included. This approach was used to first analytically compute the time coefficients for the t = 0.252s snapshot, and then reconstruct the snapshot. It was observed that the analytically computed snapshot violated the constraint. This shows that if the analytically computed snapshot violated the constraint, then so will the ROM approximated snapshot.

To allow for exact representation of the snapshot, more POD modes or modes that capture the flow structure of that snapshot should be added to the POD matrix. Alternatively, the concept of discontinuous modes proposed by Brenner *et al.* [22] can be generalized in two dimensions or three dimensions to cope with this issue. This is a topic of future research. The proposed constraining method, however, results in a system of size N+m, but only needs to be solved at the time step when the constraint is violated.

The reconstruction shown in Fig. 5 using point modes is shown in Fig. 9. It can be seen that the reconstruction is now accurate but results in an increase in the number of modes required. Increasing the number of modes increases the order of the problem along with the projection time. Efficiently incorporating these point modes needs to be investigated further.

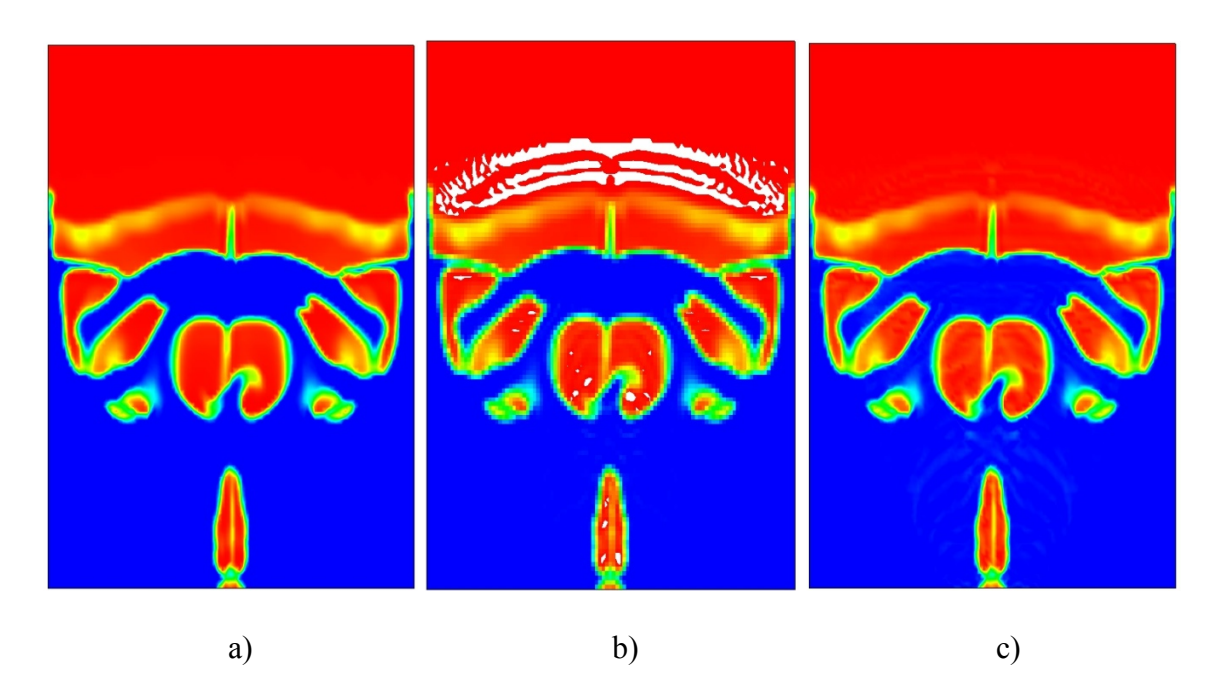


Figure 9: Void fraction reconstruction at 1s: a) FOM, b) using 86 POD modes and c) 86 POD + 719 Point Modes.

CONCLUSION

A novel constrained reduced-order methodology was developed by applying the Karush-Kuhn-Tucker conditions to the reduced-order model based on proper orthogonal

decomposition. The C-ROM was applied to the first-order wave equation where artificial errors were introduced into the model. The C-ROM was then compared to ROM under the influence of these artificial errors which caused for the error arising during the solution of the eigenvalue problem and the computation of snapshots using the full-order model. It was shown that the C-ROM is able to constrain the solution, while the ROM produces a solution that violates the user-defined constraint. The ROM was also shown to be more sensitive than the C-ROM to the propagation and compounding of error through the time domain. Finally, a C-ROM is developed for bubbling fluidized beds to constrain the gas void fraction to physically feasible bounds. Two different systems of equations, one from ROM and the other C-ROM, were shown to produce the same results when the constraint is not violated, thereby validating the methodology of C-ROM. The ability of C-ROM to constrain the gas void fraction was then investigated. It was shown that the analytically computed void fraction itself violated the constraint. Therefore, so did the C-ROM approximated void fraction. It showed that the POD basis functions must be able to capture the void fraction structure for the C-ROM to find the appropriate time coefficients. That is, for the constraint to be satisfied, such time coefficients should exist or POD modes that can lead to these time coefficients should be used. One such method of computing these POD modes is reported, but needs further investigation to be applied efficiently and in higher dimensional problems.

ACKNOWLEDGEMENTS

The lead author gratefully acknowledges the financial support from Florida International University in the form of an FIU Presidential Fellowship. Funding for this work was provided by the Department of Energy's National Energy Technology Laboratory under grant number DE-FE0023114 to FIU/ARC.

DISCLAIMER

This report was prepared as an account of work sponsored by an agency of the United States Government. Neither the United States Government nor any agency thereof, nor any of their employees, makes any warranty, express or implied, or assumes any legal liability or responsibility for the accuracy, completeness, or usefulness of any information, apparatus, product, or process disclosed, or represents that its use would not infringe privately owned rights. Reference herein to any specific commercial product, process, or service by trade name, trademark, manufacturer, or ortherwise does not necessarily constitute or imply its endorsement, recommendation or favoring by the United States Government or any agency thereof. The views and opinions of authors expressed herein do not necessarily state or reflect those of the United States Government or any agency thereof.

REFERENCES

[1] Besselink, B., Tabak, U., Lutowska, A., van de Wouw, N., Nijmeijer, H., Rixen, D.J.,

- Hochstenbach, M.E. and Schilders, W.H.A., 2013. A comparison of model reduction techniques from structural dynamics, numerical mathematics and systems and control, *Journal of Sound and Vibration*, 332, pp 4403-4422
- [2] Cangellaris, A.C., and Zhao, L., 1999. Passive reduced-order modeling of electromagnetic systems, *Computer Methods in Applied Mechanics and Engineering*, 169, pp 345-358
- [3] Gugercin, S., and Antoulas, C.A., 2004. A survey of model reduction by balanced truncation and some new results, *International Journal of Control*, 77, (8) pp 748-766
- [4] Rewienski, M. and White, J., 2003. A trajectory piecewise-linear approach to model order reduction and fast simulation of nonlinear circuits and micromachined devices, *IEEE Transactions on Computer-Aided Design of Integrated Circuits and Systems*, 22, pp 155-170
- [5] Beran, P. S. and Silva, W. A., 2001. Reduced-order modeling: New approaches for computational physics, *Proceedings of the 39th AIAA Aerospace Sciences Meeting*, *Reno, NV*.
- [6] Dowell, E.H. and Tang, D., 2003. *Dynamics of Very High Dimensional Systems*. World Scientific Publishing Company, Hackensack, NJ.
- [7] Lucia, D.J., Beran, P.S. and Silva, W.A., 2004. Reduced-order modeling: new approaches for computational physics, *Progress in Aerospace Sciences*, 40, pp 51–117
- [8] Wang, A., Li, J., Di, Z., Tian, X. and Xie, D., 2011. A new reduced stabilized mixed finite-element method based on proper orthogonal decomposition for the transient Navier-Stokes equations, *Mathematical Problems in Engineering*, Vol. 2011, Article ID 895386,

- [9] Fic, A., Bialecki, R.A. and Kassab, A.J., 2006. Solving transient nonlinear heat conduction problems by proper orthogonal decomposition and the finite-element method, *Numerical Heat Transfer, Part B: Fundamentals*, 48, pp 102-124
- [10] Yuan, T., Cizmas, P.G. and O'Brien, T., 2005. Reduced-order model for a bubbling fluidized bed based on proper orthogonal decomposition, *Computers and Chemical Engineering*, 30, pp 243-259
- [11] Luo, Z., Xie, D. and Teng, F., 2014. A POD-based reduced-order FD extrapolating algorithm for traffic flow, *Advances in Difference Equations*, 269, pp 2-13
- [12] Luo, Z., Gao, J. and Xie, Z., 2015. Reduced-order finite difference extrapolation model based on proper orthogonal decomposition for two-dimensional shallow water equations including sediment concentration, *Journal of Mathematical Analysis and Applications*, 429, pp 901-923
- [13] Amsallem, D. and Farhat, C., 2008. Interpolation method for adapting reduced-order models and application to aeroelasticity, *AIAA Journal*, 46, pp 1803–1813
- [14] Freno, B., Brenner, T.A. and Cizmas, P.G.A., 2013. Using proper orthogonal decomposition to model off-reference flow conditions, *International Journal of Non-Linear Mechanics*, 54, pp 76-84
- [15] Hay, A., Akhtar, I. and Borggaard, J.T., 2012. On the use of sensitivity analysis in model reduction to predict flows for varying inflow conditions, *International Journal of Numerical Methods in Fluids*, 68, pp 122-134
- [16] Vetrano, F., Garrec, C.L., Mortchelewicz, G.D. and Ohayon, R., 2011. Assessment of

- strategies for interpolating POD based reduced order models and application to aeroelasticity, *Journal of Aeroelasticity and Structural Dynamics*, 2, pp 85–104
- [17] Bogaers, A.E.J., Kok, S. and Malan, A.G., 2011. Highly efficient optimization mesh movement method based on proper orthogonal decomposition, *International Journal for Numerical Methods in Engineering*, 86, pp 935-952
- [18] Freno, B.A. and Cizmas, P.G.A., 2014. A proper orthogonal decomposition method for nonlinear flows with deforming meshes, *International Journal of Heat and Fluid Flow*, 50, pp 145-159
- [19] Freno, B.A., Matula, N.R., Fontenot, R.L. and Cizmas, P.G.A., 2015. The use of dynamic basis functions in proper orthogonal decomposition, *Journal of Fluids and Structures*, 54, pp 332-360
- [20] Cizmas, P.G.A., Richardson, B.R., Brenner, T.A., O'Brien, T.J. and Breault, R.W., 2008. Acceleration techniques for reduced-order models based on proper orthogonal decomposition, *Journal of Computational Physics*, 227, pp 7791–7812
- [21] Brenner, T.A., Fontenot, R.L., Cizmas, P.G.A., O'Brien, T.J. and Breault, R.W., 2012. A reduced-order model for heat transfer in multiphase flow and practical aspects of the proper orthogonal decomposition, *Computers & Chemical Engineering*, 43, pp 68–80
- [22] Brenner, T.A., Fontenot, R.L., Cizmas, P.G.A., O'Brien, T.J. and Breault, R.W., 2010. Augmented proper orthogonal decomposition for problems with moving discontinuities, *Powder Technology*, 203, pp 78–85
- [23] Alonso, D., Velazquez, A. and Vega, J.M., 2009. A method to generate computationally efficient reduced order models, *Computer Methods in Applied Mechanics*

and Engineering, 198, pp 2683-2691

[24] Holmes, P., Lumley, J. and Berkooz, G., 1996. *Turbulence, Coherent Structures, Dynamical Systems and Symmetry*, Cambridge University Press, Cambridge, UK

[25] Sirovich, L., 1987, Turbulence and the dynamics of coherent structures, *Quarterly of Applied Math*ematics, 45, pp 561–590

[26] Boyd, S. and Vanderberghe, L., 2009. *Convex Optimization*, Cambridge University Press

[27] Syamlal, M., 1998. *MFIX documentation numerical technique*. Technical Report DE-AC21-95MC31346. EG&G Technical Services of West Virginia.

APPENDIX A. HYDRODYNAMIC MODEL FOR TWO-PHASE FLUIDIZED BED

The physics of isothermal fluidized beds is governed by the laws of mass and momentum conservation. The fluidized bed was modeled using a two-fluid model (TFM) of Syamlal *et al.* [27]. In the case of no chemical reactions or physical processes such as evaporation, where no interface mass transfer occurs, the gas and solid phase mass balance equations are given as

$$\frac{\partial}{\partial t} (\varepsilon_m \rho_m) + \nabla \cdot (\varepsilon_m \rho_m \vec{v}_m) = 0 \tag{A.1}$$

where m represents the phase (gas or solid), ρ is the phase density, ε is the void fraction and \vec{v} is the velocity vector.

The gas and solid momentum balance equations are given as

$$\frac{\partial}{\partial t} (\varepsilon_m \rho_m \vec{v}_m) + \nabla \cdot (\varepsilon_m \rho_m \vec{v}_m \vec{v}_m) = -\varepsilon_m \nabla p_g + \nabla \cdot \overline{\overline{\sigma}}_m + F_{gs} (\vec{v}_s - \vec{v}_g) + \varepsilon_m \rho_m \vec{g}$$
 (A.1)

The first two terms on the right hand side represent the normal and the shear forces, respectively. The third term represents the contribution of an aerodynamic drag force due to solid particles moving with different local velocity vector than the local gas. The last term on the right hand side represents a body force due to gravity.

APPENDIX B. DERIVATION OF REDUCED SOLIDS VOLUME FRACTION CORRECTION EQUATION

The solids volume fraction correction equation can be written as

$$a_P^{\varepsilon_s} \varepsilon_{sP}^{'} = \sum_{nb} a_{nb}^{\varepsilon_s} \varepsilon_{snb}^{'} + b_P^{\varepsilon_s}$$
(B.1)

The reconstruction for the gas void fraction can be written as

$$\varepsilon_{g}(x,t) = \phi_{0}(x) + \sum_{k=1}^{m^{\varepsilon_{s}}} \alpha_{k}^{\varepsilon}(t) \phi_{k}(x)$$
 (B.2)

Then, similar to the pressure correction, the gas void fraction can be corrected as

$$\varepsilon_{g}(x,t) = \varepsilon_{g}^{*}(x) + \varepsilon_{g}(x,t) \tag{B.3}$$

where $oldsymbol{arepsilon}_g^*$ is the tentative value of the gas void fraction and $oldsymbol{arepsilon}_g^*$ is the correction.

Assuming $\phi_0(x)$ and $\varepsilon_g^*(x)$ to be equal and combining Eq. (B.2) and Eq. (B.3) yields

$$\varepsilon_{g}(x,t) = \sum_{k=1}^{m^{\varepsilon_{s}}} \alpha_{k}^{\varepsilon_{g}}(t) \phi_{k}(x)$$
 (B.4)

Dropping for convenience the ε_s superscript, replacing in Eq. (B.1) the subscript P by i and substituting Eq. (B.4) into (B.1) yields

$$\sum_{k=1}^{m} \alpha_{k} \left(a_{i} \phi_{k}(x_{i}) - \sum_{i_{nb}=1}^{NB} a_{i_{nb}} \phi_{k}(x_{i_{nb}}) \right) = b_{i}, \qquad i = 1, ..., N$$
(B.5)

Here, i_{nb} represents the neighbor of cell i, NB is the total number of neighbors of a cell, and m is the number of modes kept in the POD reconstruction. Eq. (B.5) can also be written as

$$\sum_{k=1}^{m} \alpha_{k} \left([A] \{ \phi_{k} \} - \sum_{nb=1}^{NB} [A_{nb}] \{ \phi_{k_{nb}} \} \right) = \{ b \},$$
(B.6)

where [A] and $[A_{nb}]$ are diagonal matrices with $A_{ii} = a_i$ and $A_{nb_{ii}} = a_{i_{nb}}$, i = 1,...,N, $\{\phi_k\} = \{\phi_k(x_1), \phi_k(x_2), ..., \phi_k(x_N)\}^T$ and $\{\phi_{k_{nb}}\} = \{\phi_k(x_{1_{nb}}), \phi_k(x_{2_{nb}}), ..., \phi_k(x_{N_{nb}})\}^T$. Eq. (B.6) is then projected onto the POD modes by left-multiplying it with the transposed eigenvectors $\{\phi_l\}^T$.

$$\{\phi_{l}\}^{T} \sum_{k=1}^{m} \alpha_{k} \left([A] \{\phi_{k}\} - \sum_{nb=1}^{NB} [A_{nb}] \{\phi_{k_{nb}}\} \right) = \{\phi_{l}\}^{T} \{b\}, \quad i = 1, ..., m$$
(B.7)

The resulting system is of size m with m unknowns α_i . After adding back the superscripts ε_s and ε_s , this system can be written as

$$\left[\tilde{A}^{\varepsilon_{s}}\right]\left\{\alpha^{\varepsilon_{s}'}\right\} = \left\{\tilde{B}^{\varepsilon_{s}}\right\} \tag{B.8}$$

where

$$\tilde{A}_{lk}^{\varepsilon_s} = \{\phi_l\}^T [A] \{\phi_k\} - \sum_{nh=1}^{NB} \{\phi_l\}^T [A_{nb}] \{\phi_{k_{nb}}\}, \quad l, k = 1, ..., m$$
(B.9)

and

$$\tilde{B}_{l}^{\varepsilon_{s}} = \left\{ \phi_{l} \right\}^{T} \left\{ b \right\}, \qquad l = 1, ..., m$$
(B.10)

APPENDIX C. TEST CASE FOR TWO-DIMENSIONAL FLUIDIZED BEDS PROBLEM

Figure C.1 and Table C.1 define the geometry of the fluidized bed and the applied boundary conditions. In Table C.1, Case 1 refers to the test case used to show the nonphysical results obtained using traditional ROM, while Case 2 refers to the test case used to validate the C-ROM. The snapshots are collected at a constant interval of 0.0025s, that is, M = 320. It was demonstrated that 320 snapshots were adequate to capture the dynamics of the fluidized bed [10]. In this case, the spatial grid is such that $N \approx 14000$, leading to an eigenvalue problem of size N if the method of snapshots is not used.

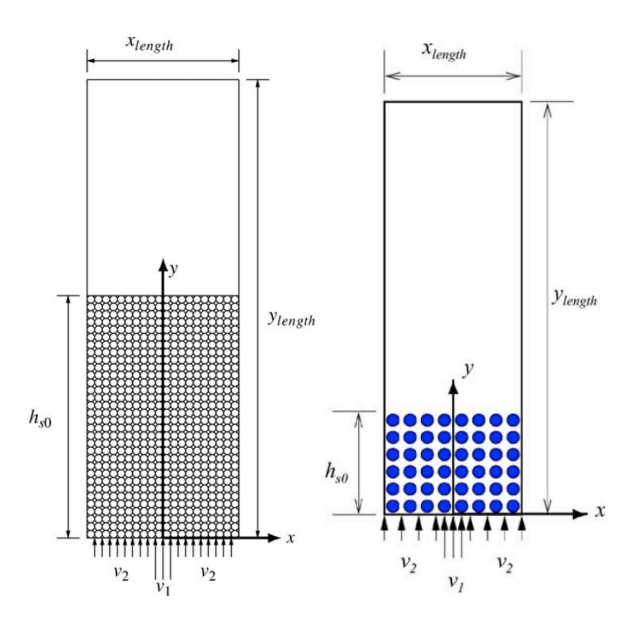


Figure C.1: Geometry and boundary conditions for two-dimensional fluidized bed used to show: a) nonphysical ROM results, and b) validated C-ROM

Table C.1.: Geometry, boundary conditions and physical properties for test case of fluidized bed

| Parameter | Description | Units | Case 1 | Case 2 |
|--------------------------|-------------------------------------|---------------------|-------------|--------------------|
| x_{length} | Length of domain in x – direction | cm | 39.37 | 25.4 |
| \mathcal{Y}_{length} | Length of domain in y – direction | cm | 58.44 | 76.5 |
| i_{max} | Number of cells in x – direction | - | 108 | 108 |
| j_{max} | Number of cells in y – direction | - | 124 | 124 |
| v_1, v_2 | Gas inflow velocities | cm/s | 355, 28.4 | 120,1 |
| p_{gs} | Static pressure at outlet | g/cm/s ² | $1.01e^{6}$ | $1.01e^{6}$ |
| T_{g0} | Gas Temperature | K | 297 | 297 |
| μ_{g0} | Gas viscosity | g/cm/s | $1.8e^{-4}$ | 1.8e ⁻⁴ |
| t_{start} | Start time | S | 0.2 | 0.2 |
| t_{stop} | Stop time | S | 1.0 | 1.0 |
| $ ho_{s0}$ | Particle density | g/cm ³ | 2.61 | 1.0 |
| D_p | Particle diameter | cm | 0.05 | 0.05 |
| h_{s0} | Initial height of packed bed | cm | 29.22 | 14.7 |
| $\mathcal{E}_{g}^{^{*}}$ | Initial void fraction of packed bed | - | 0.4 | 0.4 |

APPENDIX D. DERIVATION OF THE KKT SYSTEM OF EQUATIONS

This section provides a detailed implementation of the KKT conditions and derivation of the KKT system. Consider the system of equations for the solution of gas void fraction correction

$$\left[\tilde{A}^{\varepsilon_{s}}\right]\left\{\alpha^{\varepsilon_{s}}\right\} = \left\{\tilde{B}^{\varepsilon_{g}}\right\} \tag{D.1}$$

where the constraint, g, to be satisfied is

$$g_1 = \varepsilon^*(x) + \Phi(x)\alpha(t) - 1.0 \le 0 \tag{D.2}$$

The solution of Eq. (D.1) is analogous to the minimization of the functional

$$\min J = \left\| \tilde{A}^{\varepsilon_s} \alpha^{\varepsilon_s} - \tilde{B}^{\varepsilon_s} \right\|^2 \tag{D.3}$$

The Lagrangian can then be constructed using Eq. (26) as

$$L = J + \lambda g_1 = \left\| \tilde{A}^{\varepsilon_s} \alpha^{\varepsilon_s} - \tilde{B}^{\varepsilon_g} \right\|^2 + \lambda^T \left(\varepsilon^* + \Phi \alpha - 1.0 \right)$$
 (D.4)

where λ are the KKT multipliers. Applying the stationary condition to the Lagrangian yields

$$\frac{\partial L}{\partial \alpha} = L_{\alpha} = 2(\tilde{A}^{\varepsilon_s})^T \tilde{A}^{\varepsilon_s} \alpha^{\varepsilon_s} - 2(\tilde{A}^{\varepsilon_s})^T \tilde{B}^{\varepsilon_s} + \Phi^T \lambda = 0$$
 (D.5)

When applying the KKT conditions, the inequality constraint must be treated as a binding constraint (that is, $g_1 = 0$). This then allows the complementary slackness condition to be

written as

$$\varepsilon^* + \Phi\alpha - 1.0 = 0 \tag{D.6}$$

The KKT system can then be written as

$$\begin{pmatrix}
2(\tilde{A}^{\varepsilon_s})^T \tilde{A}^{\varepsilon_s} & \Phi^T \\
\Phi & 0
\end{pmatrix}
\begin{cases}
\underline{\alpha}^{\varepsilon_g} \\
\underline{\lambda}
\end{cases} = \begin{cases}
2(\tilde{A}^{\varepsilon_s})^T \tilde{B}^{\varepsilon_g} \\
1.0 - \varepsilon_g^*
\end{cases}$$
(D.7)

VITAE



Sohail R. Reddy (M.Sc.'15 and B.Sc.'14, FIU) is a Ph.D. candidate in the MAIDROC Laboratory at Florida International University (FIU). He is the recipient of FIU Presidential Fellowship, FIU Most Outstanding Masters Degree Graduate 2015 award and four international ASME awards in the field of design, CFD and electronics packaging. He currently works on developing reduced order modeling for chemically reacting flows in fluidized beds, inverse problems in materials science, cooling of high heat flux electronics and electrohydrodynamics in two-phase flows. He previously worked as a research assistant at the FIU-Applied Research Center in Miami, Florida.



Brian Freno is a Senior Member of the Technical Staff in the Verification, Validation, Uncertainty Quantification, and Credibility Processes Department at Sandia National Laboratories in Albuquerque, NM, where he conducts research in reduced-order modeling and code verification for fluid and solid mechanics. Brian obtained his PhD, MS, and BS in Aerospace Engineering from Texas A&M University, where he received the Outstanding Doctoral Student Award and the Outstanding Achievement Award for Aerodynamics and Propulsion. He has previously worked for Lockheed Martin Missiles and Fire Control, the NASA Marshall Space Flight Center, and Halliburton.



Paul Cizmas is a Professor in the Department of Aerospace Engineering at Texas A&M University. He is actively conducting research in propulsion, aeroelasticity, and computational fluid dynamics. Paul obtained his Ph.D. from Duke University and his Dipl. Ing. from the Bucharest Polytechnic Institute. He has previously worked for Westinghouse Science and Technology Center in Pittsburgh, PA.



Seckin Gokaltun is a Research Scientist at Kingsbury Inc. and an Adjunct Faculty at Drexel University. His expertise is in computational fluid dynamics, multiphase flows and microscale heat transfer. Seckin received his B.S. in Aeronautical Engineering from Middle East Technical University and Ph.D. in Mechanical Engineering from Florida International University. He also has a M.S. in Computational Science and Engineering from Istanbul Technical University. Previously he worked at Applied Research Center of FIU where he served as the Principal Investigator of research grants funded by DOE-NETL.



Dwayne McDaniel is Senior Research Scientist at the Applied Research Center of Florida International University. He is the Principal Investigator and Project Manager for a number of current projects funded by DOE-EM, DOE-NETL, the FAA and ONR. Areas of research include composites, structural mechanics, computational fluid mechanics and robotics. He received his Ph.D., M.S. and B.S. from the Aerospace, Engineering Mechanics and Engineering Science Department at the University of Florida. He is also a registered professional engineer in the State of Florida.



George S. Dulikravich (Ph.D.'79, Cornell; M.Sc.'75, Minnesota; Dipl. Ing.'73, Belgrade) Fellow ASME, AAM, RAeS. An NRC associate fellow at NASA LeRC, a visiting scientist at DFVLR-Goettingen, and a faculty at University of Texas-Austin ('82-'86), Pennsylvania State University ('86-'99), Univ. of Texas at Arlington ('99-'03). Since 2003, he is a professor and director of MAIDROC Lab in the Dept. of Mech. and Materials Eng. at the Florida International Univ. (FIU). He has over 500 highly multi-disciplinary publications in the fields spanning aerospace, mechanical, biomedical, industrial, materials and chemical engineering. In 1994, he founded *Inverse Problems in Engineering* journal.